Alloying effect on the oxidation behavior of a ductile Al0.5Cr0.25Nb0.5Ta0.5Ti1.5 refractory high-entropy alloy

Materials Today Advances 7 (2020) 100104

Contents lists available at ScienceDirect

Materials Today Advances

journal homepage: www.journals.elsevier.com/materials-today-advances/

Alloying effect on the oxidation behavior of a ductile $Al_{0.5}Cr_{0.25}Nb_{0.5}Ta_{0.5}Ti_{1.5}$ refractory high-entropy alloy

S. Sheikh [a, d], L. Gan [a, d], A. Ikeda [a], H. Murakami [a, b, **], S. Guo [c, *]

[a] National Institute for Materials Science, Sengen 1-2-1, Tsukuba, Ibaraki, 305-0047, Japan
[b] Department of Nanoscience and Nanoengineering, Waseda University, 3-4-1 Okubo Shinjuku, Tokyo, 169-8555, Japan
[c] Industrial and Materials Science, Chalmers University of Technology, 41296, Göteborg, Sweden

ARTICLE INFO

Article history:
Received 25 May 2020
Received in revised form
22 June 2020
Accepted 26 June 2020
Available online 20 August 2020

Keywords:
Refractory alloys
High-entropy alloys
Ductility
Oxides
Nitrides

ABSTRACT

Refractory high-entropy alloys (RHEAs) are widely studied because of their promising potential for ultrahigh-temperature applications. One key challenge towards the development of RHEAs as high-temperature structural materials is to concurrently achieve optimum oxidation resistance and mechanical properties. Here in this work, the effect of alloying on the oxidation behavior of ductile RHEAs was studied. Specifically, a ductile RHEA, $Al_{0.5}Cr_{0.25}Nb_{0.5}Ta_{0.5}Ti_{1.5}$, was alloyed with Al and Zr aiming to improve its oxidation resistance. The two modified RHEAs, $Al_{0.75}Cr_{0.25}Nb_{0.5}Ta_{0.5}Ti_{1.5}$ and $Al_{0.5}Cr_{0.25}Nb_{0.5}Ta_{0.5}Ti_{1.5}Zr_{0.01}$, indeed show enhanced oxidation resistance at 800 °C and 1,100 °C, compared with $Al_{0.5}Cr_{0.25}Nb_{0.5}Ta_{0.5}Ti_{1.5}$. In addition, all three RHEAs studied here show an excellent oxidation resistance at 800 °C compared with other RHEAs, although there is still a large space to further improve their performance at 1,100 °C. Internal oxidation and even nitridation are still present after oxidation exposure, indicating further efforts are required to form protective oxide scales on the surface of ductile RHEAs. Nevertheless, the work is expected to shed some light on future directions of improving the oxidation of ductile RHEAs, via the alloying route.

1. Introduction

Refractory high-entropy alloys (RHEAs) [1–3], consisting of refractory metals with high melting points, constitute one particular group of high-entropy alloys (HEAs) [4–6]. Ever since their first emergence, RHEAs have been regarded as potential next-generation high-temperature materials to break through the operating temperature limit of the state-of-the-art materials such as nickel-based superalloys [2,7]. In recent years, RHEAs have gained increasing attention because of their inherent high strength and softening resistance at elevated temperatures, surpassing those of commercialized superalloys such as Haynes 230 and Inconel 718 [1,3,8]. However, despite these advantages, RHEAs suffer from room-temperature brittleness and/or insufficient oxidation resistance, and RHEAs that possess a balanced ductility and decent oxidation resistance are simply non-existing [3]. Comparatively, brittleness is less an issue, as recently it has been proved that ductile RHEAs can be achieved using electron theory [9] or phase transformation [10]; oxidation resistance is much more challenging for RHEAs, and literature survey has indicated that most reported RHEAs are prone to catastrophic oxidation and/or embrittlement via internal oxidation, on high-temperature exposure [3,11], similar to conventional refractory elements and alloys [7,12]. To quote a few examples here, $NbCrMo_{0.5}Ta_{0.5}TiZr$ after 100 h exposure at 1,000 °C forms complex oxides with an exceptionally high mass gain of 120 mg/cm^2 [13]; AlCrMoTiW containing about 80 at.% of refractory elements shows a parabolic oxidation kinetics during 40 h of exposure to air at 1,000 °C with the mass gain of ~ 7.8 mg/cm^2, significantly higher than that of Ni-based superalloys [14,15]; AlCrNbMoTi changes its oxidation kinetics from nearly parabolic to linear behavior at 1,000 °C with the mass gain of ~ 28 mg/cm^2 after 95 h of exposure, whereas AlCrNbMo suffers from the complete oxidation at 1,000 °C after 48 h of exposure and no remaining material could be found [16]; $Al_{0.5}CrNbMoV$ shows the linear oxidation kinetics at 1,300 °C and the presence of V is detrimental to oxidation resistance with a significant mass gain of ~ 340 mg/

* Corresponding author.
** Corresponding author.
E-mail addresses: murakami.hideyuki@nims.go.jp (H. Murakami), sheng.guo@chalmers.se (S. Guo).
[d] These authors contributed equally to this work.

https://doi.org/10.1016/j.mtadv.2020.100104

cm^2 in just 20 h of exposure [17]. Efforts to improve the oxidation resistance of RHEAs have been mainly relied on alloying with Al, Cr, or Si to promote the formation of protective oxide scales like Cr_2O_3, Al_2O_3, SiO_2, or in some cases by surface treatments like pack cementation aluminizing [11,18–20]. The situation becomes even more challenging when one attempts to improve the oxidation of RHEAs while also expecting the RHEAs to possess good ductility. Indeed, most existing investigations to improve the oxidation resistance of RHEAs have not been dedicated to ductile RHEAs, which are certainly limited but available [9,21–23]. Considering the difficulty to ductilize a material that is oxidation resistant, but intrinsically brittle, it is relatively easier to improve the oxidation resistance of a material that is intrinsically ductile but insufficiently oxidation resistant, thereby motivating our work to start from ductile RHEAs.

$Al_{0.5}Cr_{0.25}Nb_{0.5}Ta_{0.5}Ti_{1.5}$ [11] is a modified alloy derived from ductile but pesting susceptible $Hf_{0.5}Nb_{0.5}Ta_{0.5}Ti_{1.5}Zr$ [9]. It is ductile at room temperature and not subject to pesting after oxidation at 800 °C for 5 h, but it gets embrittled after oxidation at 800 °C for 5 h [11] and it also suffers from pesting after 20 cyclic oxidations at 1,100 °C [24]. We previously managed to improve the oxidation resistance of $Al_{0.5}Cr_{0.25}Nb_{0.5}Ta_{0.5}Ti_{1.5}$ via a tailor-made two-step aluminizing route, by successfully forming protective Al_2O_3 scale on its surface [24]. Here in this work, we attempt to improve the oxidation resistance of this alloy via the alloying way, also hoping to achieve some generic understanding on how alloying can lead to the formation of protective surface oxide scales on ductile RHEAs. We basically made two attempts here, starting with increasing the Al content and hoping to enable the formation of protective Al_2O_3 scale, while keeping in mind that Al tends to form strong bonds with other refractory elements and excessive Al content would result in undesirable brittleness [25,26]. In the end, we focused on a modified alloy, $Al_{0.75}Cr_{0.25}Nb_{0.5}Ta_{0.5}Ti_{1.5}$, with slightly increased Al content while maintaining the room-temperature ductility. The other attempt was to add a limited amount of Zr, to study the effect of Zr addition on the oxidation resistance of $Al_{0.5}Cr_{0.25}Nb_{0.5}Ta_{0.5}Ti_{1.5}$. The inspiration is that the oxidation resistance of TiAl and Ti–15Al–2Nb gets improved after Zr alloying [27,28]. As Zr is also an active element that can form secondary phases that would deteriorate the room temperature ductility, here we worked with a modified alloy, $Al_{0.5}Cr_{0.25}Nb_{0.5}Ta_{0.5}Ti_{1.5}Zr_{0.01}$, with a rather minor addition of Zr. We expect to gain further insights into the oxidation behavior of ductile RHEAs by studying these three chosen alloys, targeting at understanding the formation of outer oxide layers, and how the oxidation proceeds inside the bulk of the materials, in case the formed oxide layers are not protective enough against oxygen ingress [12]. Specifically, we studied the oxidation behavior of these three RHEAs at 800 °C and 1,100 °C after 100 h of exposure, and we analyzed the formed oxidation products and their microstructure.

2. Experimental

RHEAs with the nominal compositions, $Al_{0.5}Cr_{0.25}Nb_{0.5}Ta_{0.5}Ti_{1.5}$, $Al_{0.75}Cr_{0.25}Nb_{0.5}Ta_{0.5}Ti_{1.5}$, and $Al_{0.5}Cr_{0.25}Nb_{0.5}Ta_{0.5}Ti_{1.5}Zr_{0.01}$, were prepared from high purity (>99.9%) elemental materials by using arc melting in a Ti-gettered Ar atmosphere on a water-cooled copper plate. For simplicity, these three RHEAs will be designated as $Al_{0.5}$, $Al_{0.75}$, and $Al_{0.5}Zr_{0.01}$, respectively. Melted button ingots were flipped and remelted at least six times to ensure chemical homogeneity. The button ingots were later melted again and subjected to drop-casting to form rectangular bars with dimensions of 40 mm (length) × 10 mm (width) × 10 mm (thickness). After casting, rectangular specimens with dimensions of 5 mm × 10 mm × 10 mm were cut from the drop-cast ingots. Continuous oxidation tests were conducted in a thermogravimetric analyzer (TGA, TAG 24, Setaram) at 800 °C and 1,100 °C in dry air with a flow rate of 150 mL/min. Specimens were heated up to the target temperatures at a rate of 15 °C/min, held at the temperature for 100 h, and subsequently cooled to room temperature at a rate of 10 °C/min. Short-term oxidation tests were also conducted at 800 °C for 1 h for all three alloys in a box furnace (MSFT-1560-P, Nikkato) under static laboratory air. Weight change was determined using an analytical balance with an accuracy of 0.01 mg. The phase constitutions were identified on the surface of specimens by X-ray diffraction (XRD, MiniFlex 600, Rigaku), using Cu–K_α radiation. Microstructure and chemical compositions of both as-cast and oxidized specimens were studied on the cross-section of specimens using a scanning electron microscope (SEM, JSM-7200F, JEOL) equipped with electron backscatter diffraction (EBSD) detector and energy dispersive spectrometer (EDS). Before metallography preparation, oxidized specimens were coated with Cu with a thickness of ~ 100 μm to protect the oxidized layers from any damage arising from cutting, grinding, and polishing. For the coating process, the RHEA specimens were fixed as the cathode, whereas Cu plates were set as the anode in the bath, which contained a saturated $CuSO_4$ solution with pH ~ 5, adjusted via H_2SO_4. A current density of ~ 0.2 A/dm^2 was used for plating with a total plating duration of 8 h. The cross-sections of the oxidized specimen were also studied with an electron probe microanalyzer (EPMA, type 1610, Shimadzu), under an acceleration voltage of 15 kV.

3. Results

3.1. Starting materials

Fig. 1(a) shows the EBSD inverse pole figure (IPF) map of the $Al_{0.5}$ alloy, exhibiting a single phase with polygrained microstructure. The corresponding XRD pattern is shown in Fig. 1(b) and it confirms that this alloy comprises a single body-centered cubic (bcc) phase, as was also reported in our earlier studies [11]. EBSD IPF maps and XRD patterns for $Al_{0.75}$ (Fig. 1(c) and (d)), and $Al_{0.5}Zr_{0.01}$ (Fig. 1(e) and (f)) also indicate the formation of a single bcc phase and polygrained microstructure in these two alloys. Interestingly, the $Al_{0.5}Zr_{0.01}$ alloy appears to have the most coarse-grained microstructure (Fig. 1(e)).

3.2. Oxidation behavior

The oxidation results for three RHEAs at 800 °C (solid lines) and 1,100 °C (dashed lines) are given in Fig. 2(a), showing the mass change (mg/cm^2) as a function of time (h). For the comparison purpose, the mass change versus time plots for several previously reported RHEAs that were oxidized at 800 °C and 1,100 °C are superimposed onto those from this work in Fig. 2(b).

For the oxidation at 800 °C, Fig. 2(a) indicates that the mass gain of $Al_{0.5}$ (1.255 mg/cm^2) has the highest weight gain, whereas $Al_{0.75}$ (0.803 mg/cm^2) has the lowest one. In addition, all three RHEAs show parabolic oxide growth during their complete exposure time at 800 °C, suggesting that the oxygen ingress is effectively limited, with the oxidation rate controlled by diffusion [13]. The mass gain versus time plots can be modeled by the oxide growth law, using the equation $\Delta m = (k_p t)^n$, where Δm is the specific mass gain, k_p is oxide growth rate constant, t is time, and n is the time exponent which can be fixed to 0.5 for a typical parabolic oxidation behavior [29]. Using the linear regression analysis, the oxide growth rate constant k_p for $Al_{0.5}$ is 0.18 $mg^2/(cm^4\ s)$, which slightly reduced to k_p = 0.17 $mg^2/(cm^4\ s)$ on Zr addition for $Al_{0.5}Zr_{0.01}$, and further reduced to 0.12 $mg^2/(cm^4\ s)$ on Al addition for $Al_{0.75}$. The oxidation kinetics analysis indicates that Al and Zr alloying helps to improve the oxidation resistance of $Al_{0.5}$, although the improvement is

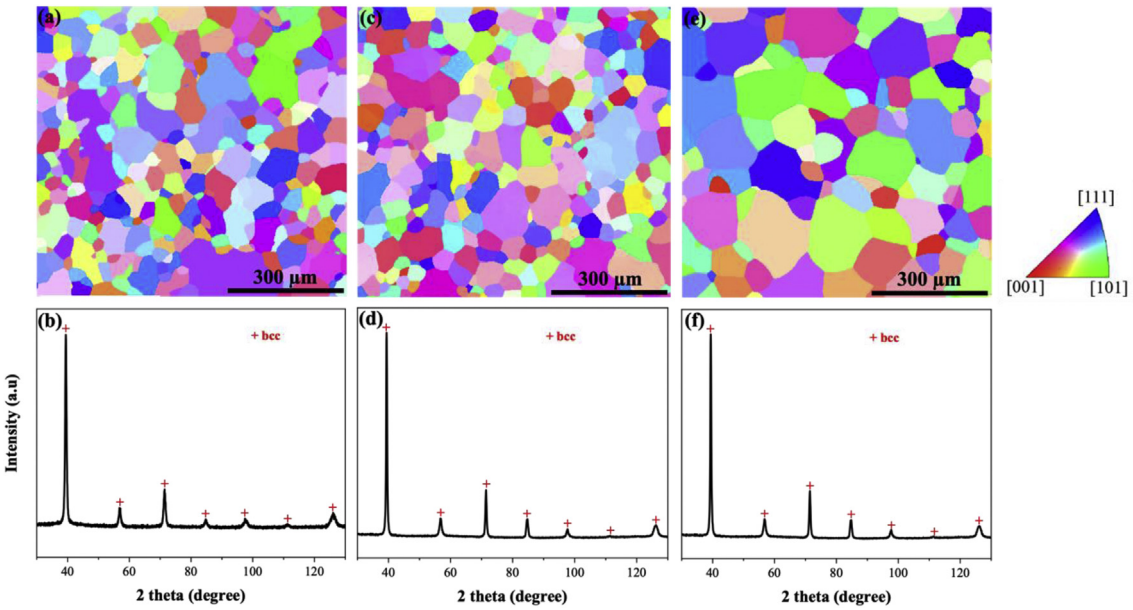

Fig. 1. EBSD IPF maps and their corresponding XRD patterns of the as-cast RHEAs. (a) and (b) are for $Al_{0.5}$, (c) and (d) are for $Al_{0.75}$, and (e) and (f) are for $Al_{0.5}Zr_{0.01}$.

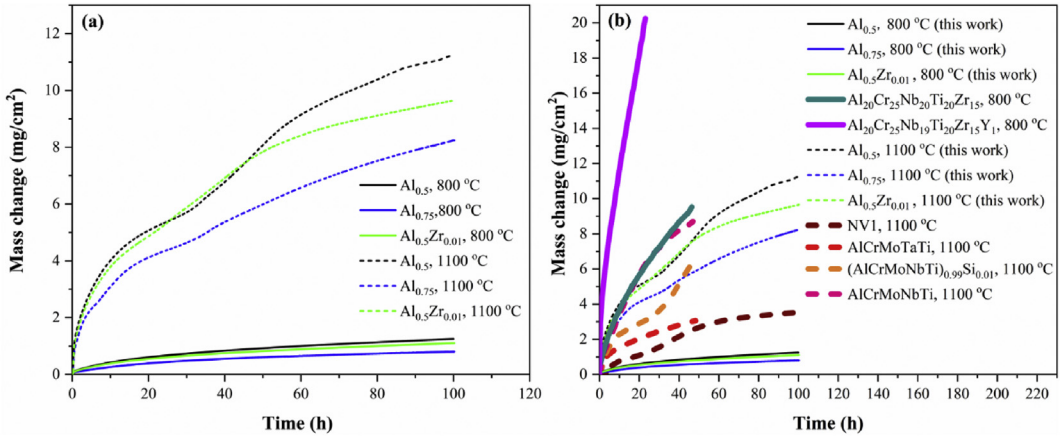

Fig. 2. (a) Specific mass change versus time plots for $Al_{0.5}$, $Al_{0.75}$, and $Al_{0.5}Zr_{0.01}$ at 800 °C (solid lines) and 1,100 °C (dotted lines); (b) comparison of specific mass change versus time between studied RHEAs in this work and selected RHEAs from the literature.

rather insignificant, in agreement with the mass gain versus time plots shown in Fig. 2(a). Nevertheless, what is significant here is that all three RHEAs exhibit much lower mass gain at 800 °C, compared with previously reported RHEAs, for example, $Al_{20}Cr_{25}Nb_{20}Ti_{20}Zr_{15}$ and $Al_{20}Cr_{25}Nb_{19}Ti_{20}Zr_{15}Y_1$ [30], as indicated by thick solid lines in Fig. 2(b).

Similar to the case at 800 °C, the $Al_{0.5}$ alloy also shows the highest mass gain (10.591 mg/cm^2) at 1,100 °C (Fig. 2(a)), whereas $Al_{0.5}Zr_{0.01}$ shows lower (9.653 mg/cm^2) and $Al_{0.75}$ shows the lowest (8.243 mg/cm^2) one among the three RHEAs. However, different to the all-the-way parabolic behavior as is the case at 800 °C, all three RHEAs at 1,100 °C experience a multistage oxidation behavior, starting from parabolic, transitioning to linear one after 20–30 h depending on individual compositions, and changing back to parabolic behavior again after 30–50 h, which is indicative of the non-stability of formed oxide scales in these alloys. Comparing the oxidation resistance of the three studied RHEAs at 1,100 °C with previously reported RHEAs (thick dashed lines in Fig. 2(b)), they are still superior to, for example, AlCrMoNbTi [18]. In addition, $Al_{0.75}$ shows superior oxidation resistance to $(AlCrMoNbTi)_{0.99}Si_{0.01}$ after 40 h of exposure [18]. However, seen from Fig. 2(b), all the three RHEAs studied here show much inferior oxidation resistance to AlCrMoTaTi [19] and an NV1 RHEA [31], which comprises Al, Cr, Nb, Mo, Ta, Ti, and Si, with much reduced Ti content than the other reported RHEAs. Notably, the NV1 alloy forms a complex oxide, $CrTaO_4$, which is claimed to lead to its enhanced oxidation resistance [31,32]. More discussions regarding the effect of formed oxides on the oxidation behavior of RHEAs will be covered in the following sections. The oxidation behavior of the three RHEAs at 800 °C and 1,100 °C will be further analyzed below, with detailed information provided from oxidation products and their composition and microstructure.

3.2.1. Oxidation at 800 °C

XRD patterns from the three RHEAs after oxidation at 800 °C are shown in Fig. 3(a). All the three RHEAs show the formation of TiO_2 (space group: $P4_2/mnm$, No. 136), which is understandable as Ti is present in the highest proportion in all of them; Ti_2AlNb (space

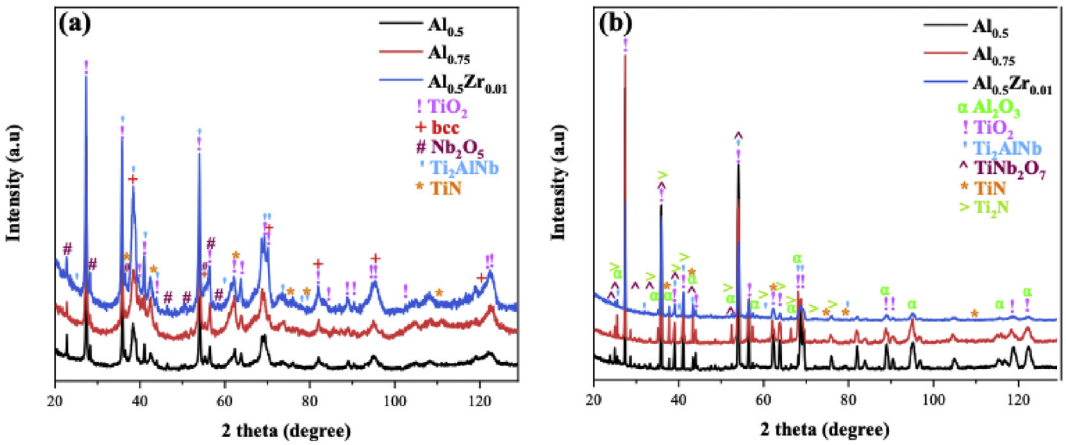

Fig. 3. XRD patterns of $Al_{0.5}$, $Al_{0.75}$, and $Al_{0.5}Zr_{0.01}$ specimens after 100 h of exposure at (a) 800 °C and (b) 1,100 °C.

group: Pm-3m, No. 221), Nb_2O_5 (space group: P-3, No. 147), and a nitride phase TiN (space group: Fm-3m, No. 225) are also detected, implying that these RHEAs are susceptible to not only oxygen but also nitrogen attack. A note can be added here that, based on the literature, the diffusion rate of oxygen in Ti_2AlNb, at 800 °C, is significantly high and it can result in the formation of oxides such as TiO_2, Al_2O_3, and Nb_2O_5 [33]. Although the XRD patterns were collected on the surface, the bcc phase from the substrates was also detected, indicating the limited thickness of the formed oxides.

Fig. 4 shows representative microstructures of the three RHEAs after 100 h of oxidation at 800 °C. The outer oxide scale formed on $Al_{0.5}$ is rather continuous and contains varying compositional contrast as shown in Fig. 4(a), echoing the formed multiple oxides seen in Fig. 3(a). The substrate remains the polygrained microstructure (Fig. 4(b)), and internal oxidation (Fig. 4(a) and (c)) is seen

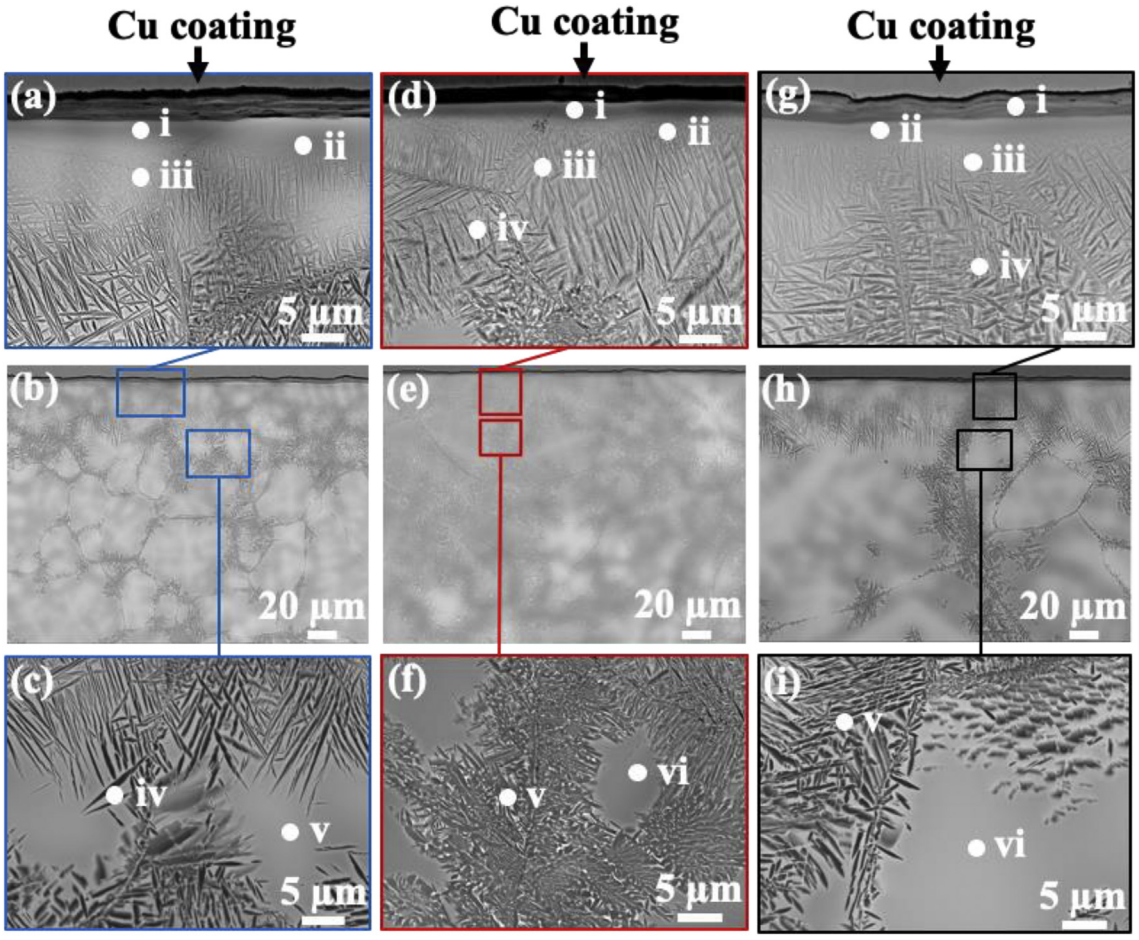

Fig. 4. Cross-sectional microstructures of (a–c) $Al_{0.5}$, (d–f) $Al_{0.75}$, and (g–i) $Al_{0.5}Zr_{0.01}$ specimens after 100 h of exposure at 800 °C.

within the substrate. Needle-like features are seen to distribute densely near the outer layer, both within the grains and along grain boundaries. Deeper into the bulk of the substrate material, both the number density and size of these needle-like features decrease, and they distribute mostly along the grain boundaries. These observations indicate that under the current exposure condition, diffusion through grain boundary and grains is quite pervasive [34]. The degree of internal oxidation is semiquantitatively characterized by compositional analysis using SEM–EDS, bearing in mind that the limitation of this technique for oxygen content measurement. The sampled positions are indicated in Fig. 4(a) and (c), and their compositions are given in Table 1. The oxygen content basically decreases rather quickly from ~ 60 at.% near the outer layer to ~8 at.% inside the bulk of the substrate. Nitrogen-rich regions are also seen just below the outer layer, thus confirming that nitrogen diffuses into the substrate, possibly forming TiN as the XRD results indicate. Similarly, the morphology of the outer layer and internally formed oxides/nitrides for $Al_{0.75}$ and $Al_{0.5}Zr_{0.01}$ can be seen in Fig. 4(d–f) and (g–i), respectively, and the compositional information is provided in Table 1. Internal oxidation exists in all cases, but Table 1 suggests that the oxygen dissolution in $Al_{0.75}$ shows the most distinct trend of decrease from near the surface to inside the substrate, which is encouraging and indicates that a higher Al content could be effective in minimizing the oxygen ingress. In addition, nitrogen is seen to be enriched at a short distance below the outer oxide layer, and the enrichment is also most insignificant in the case of $Al_{0.75}$, thus indicating a possible connection between the severity of internal oxidation and nitridation.

A short oxidation at 800 °C for 1 h was also made on all the three RHEAs, to see how the oxidation evolves. Fig. 5(a) and (b), (c) and (d), and (e) and (f) show the microstructure of $Al_{0.5}$, $Al_{0.75}$, and $Al_{0.5}Zr_{0.01}$, respectively, after oxidation at 800 °C for 1 h. In all cases, the outer layers are only partially oxidized and underneath it, there is some indication of internal oxidation, but the severity is almost negligible if compared to the cases after 100 h of oxidation at this temperature. Needle-like features, therefore the products of internal oxidation, are seen just below the outer layer and distributing along the grain boundaries further into the bulk of the substrate. The chemical compositions with respect to the relative depth from the outer layer, measured from regions that are indicated in Fig. 4(b), (d) and (f), are given in Table 2. Naturally, in all cases, the oxygen content decreases from the outer layer to within the bulk of the material, where still a significant portion is free from any internal oxidation. It is again noted that the $Al_{0.75}$ alloy shows the lowest oxygen dissolution along the depth direction, confirming that the oxide layer formed in it is most effective in limiting the oxygen ingress into the substrate. Importantly, nitrogen is not detected in all cases, which suggests that nitrogen ingress only occurs at a later stage.

Table 1
SEM–EDS analysis for the oxidized specimens after 100 h of exposure at 800 °C. The sampled locations are shown in Fig. 4 (a) and (c), (d) and (f), and (g) and (i), respectively.

Composition	Element (at. %)							
Location	Al	Cr	Nb	Ta	Ti	N	O	Zr
$Al_{0.5}$								
i	4.51	3.66	5.24	4.95	19.15	4.31	58.18	–
ii	7.6	4.25	10.12	13.31	24.01	15.27	25.44	–
iii	7.94	5.26	8.34	9.06	29.42	24.92	15.06	–
iv	15.03	4.13	9.23	10.44	53.71	–	7.46	–
v	9.96	6.16	14.84	21.25	39.63	–	8.16	–
$Al_{0.75}$								
i	11.51	3.67	3.17	3.18	16.15	0.89	61.44	–
ii	11.35	4.44	8.09	8.61	25.84	18.45	23.23	–
iii	15.79	6.5	11.06	11.27	42.3	1.26	11.82	–
iv	16.32	6.48	11.05	12.2	43.55	0.67	9.73	–
v	18.93	3.45	13.18	11.01	47.49	–	5.94	–
vi	16.73	7.16	13.61	14.59	44.83	–	3.08	–
$Al_{0.5}Zr_{0.01}$								
i	4.3	2.89	1.51	1.29	16.46	0.28	72.9	0.38
ii	5.29	3.99	5.18	4.59	17.46	4.6	58.89	–
iii	7.93	4.68	7.58	7.83	24.83	23.92	23.23	–
iv	12.86	8.84	11.12	9.55	45.73	–	11.83	0.07
v	12.03	9.72	12.57	12.03	44.87	–	8.77	–
vi	11.89	6.44	14.89	18.72	44.78	–	3.28	–

3.2.2. Oxidation at 1,100 °C

XRD patterns for the three RHEAs after oxidation at 1,100 °C for 100 h are given in Fig. 3(b). TiO_2 and Ti_2AlNb, which are also seen in the alloys after oxidation at 800 °C, are still present. Additional peaks from $TiNb_2O_7$ (space group: P12/m1, No. 10) phase are seen, which is formed because of the reaction between Nb and TiO_2 at this temperature and this has been reported in the oxidation studies of other RHEAs as well [12,35]. $TiNb_2O_7$ can also be written as $TiO_2 \cdot Nb_2O_5$ because of the solubility of Nb_2O_5 in TiO_2 ranges between 2 at. % and 41 at. % [36]. Peaks from a stable oxide α-Al_2O_3 (space group: R-3c, No. 167) are seen for all the three RHEAs, with the peak intensity strongest for $Al_{0.75}$. In addition, two types of nitrides are detected: TiN and Ti_2N (space group: $P4_2/mnm$, No. 136). The absence of the bcc phase from the substrate is apparently due to the thicker oxide layer that is formed beyond the penetration depth of the X-ray.

The microstructures of the three RHEAs after 100 h of oxidation at 1,100 °C are shown in Fig. 6. An oxide layer with various compositional contrast can be seen to form on all the three RHEAs, corresponding to the formed multiple oxides according to the XRD results (Fig. 3(b)). An intermediate region, containing various lamellar and blocky features, forms between the outer oxide layer and the substrate, which is at least not obvious for the case of oxidation at 800 °C. Underneath the intermediate region comes the substrate, and it is apparently not free from internal oxidation or nitridation. Considering the limitation of SEM–EDS to measure light elements like O and N, semiquantitative chemical analyses were made at different locations on the three RHEAs, as indicated in Fig. 6(a–c) and the results are given in Table 3. The oxygen content decreases rather gradually in $Al_{0.5}$, from the oxide layer to the intermediate region and to the substrate, but its decrease tendency is significantly faster in $Al_{0.75}$ and $Al_{0.5}Zr_{0.01}$, indicating that the formed oxide layer in $Al_{0.75}$ and $Al_{0.5}Zr_{0.01}$ are much more effectively limiting the oxygen ingress. Nitrogen is also seen in all cases, and it is enriched in the intermediate region while limited in the oxide layer. As Ti has the highest proportion in all the three RHEAs, by combining the XRD results in Fig. 3(b) and the compositional information in Table 3 and the previous knowledge on the oxidation behavior of Ti alloys, it is reasonable to assume that the oxide layer contains TiO_2 and Al_2O_3, the combination of which is known to be not highly protective when compared to the ideal case where Al_2O_3 is formed exclusively [37], and possibly also $TiNb_2O_7$; the intermediate region shall contain Ti_2AlNb and also the nitrides Ti_2N and TiN. The sampled location ii in the $Al_{0.75}$ alloy corresponds nicely to TiN, and the same statement can be rather safely made for the sampled location ii in $Al_{0.5}$; as will be shown later, nitrides are also seen further into the bulk of the substrate. For example, the sampled location iii in the $Al_{0.5}Zr_{0.01}$ alloy seems to correspond to Ti_2N, according to the compositional information in Table 3. The sequence of forming various oxides and nitrides along with their corresponding microstructures at different depths within the oxide layer, intermediate region, and the substrate, is possibly due to the change of local partial pressure of nitrogen and oxygen [35].

Fig. 7 shows the SEM–EDS elemental mapping for the three alloys, after oxidation at 1,100 °C for 100 h. Thick oxide layers are

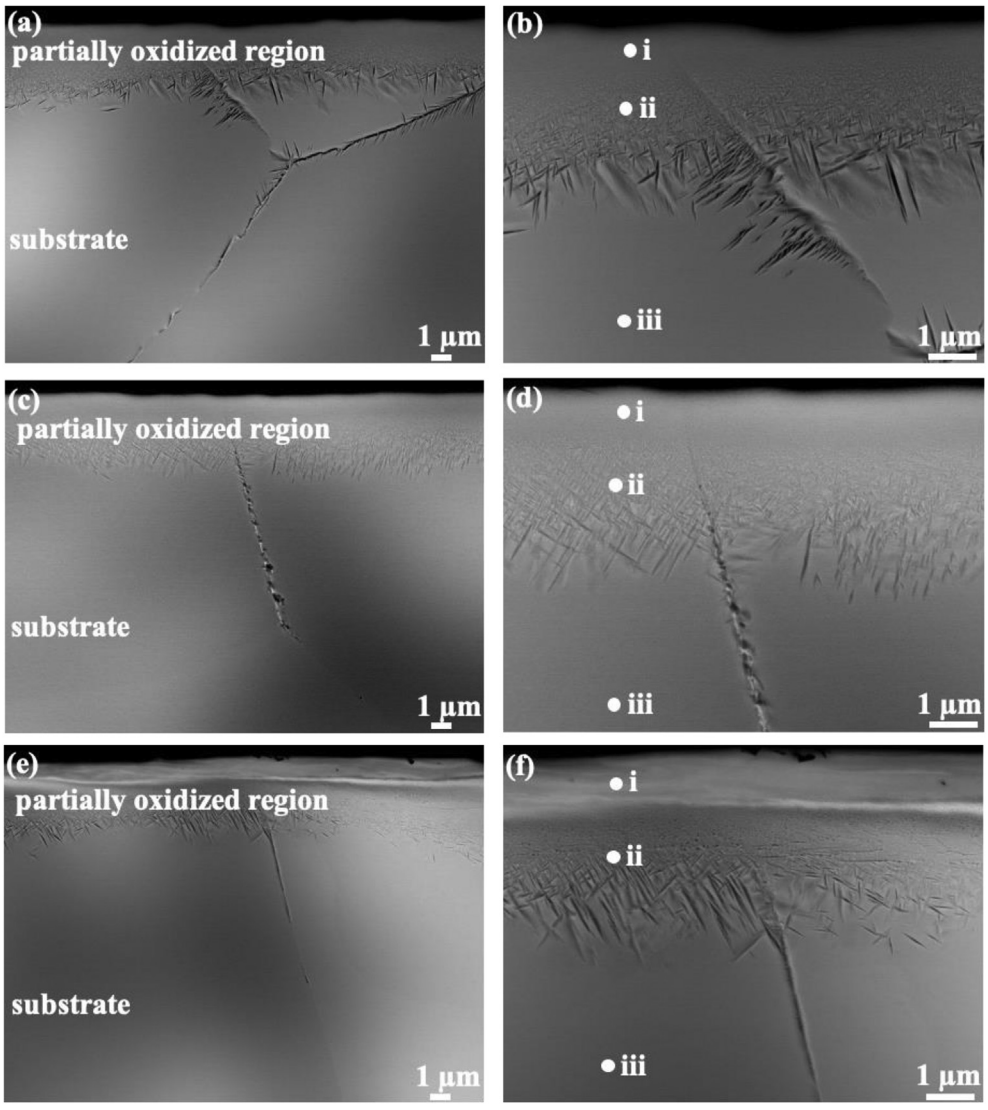

Fig. 5. Cross-sectional microstructures of specimens (a–b) $Al_{0.5}$, (c–d) $Al_{0.75}$, and (e–f) $Al_{0.5}Zr_{0.01}$ after short-term exposure at 800 °C for 1 h.

Table 2
SEM–EDS analysis for the oxidized specimens after short-term exposure at 800 °C for 1 h. The sampled locations are shown in Fig. 2(b), (d), and (f).

Composition	Element (at. %)						
Location	Al	Cr	Nb	Ta	Ti	O	Zr
$Al_{0.5}$							
i	11.2	6.78	10.87	10.81	38.6	21.74	–
ii	11.75	7.57	11.91	12.45	43.62	12.7	–
iii	13.11	7.61	13.61	13.68	45.81	6.18	–
$Al_{0.75}$							
i	15.89	6.43	11.02	11.75	37.41	17.5	–
ii	17.48	7.42	12.41	11.81	42.71	8.17	–
iii	18.52	8.1	12.31	11.02	46.12	3.92	–
$Al_{0.5}Zr_{0.01}$							
i	9.74	5.66	11.1	12.27	35.13	26.1	–
ii	12.7	7.96	12.15	11.19	46.79	9.15	0.06
iii	13.36	9.28	11.78	10.18	49.96	5.37	0.07

clearly visible, seen from Fig. 7(h), (p), and (x). A closer inspection of the oxide layer for each RHEA reveals the presence of multiple layers in it, and the outer layer is a very thin layer enriched in Al, which shall correspond to Al_2O_3. Ti is in general enriched in the whole oxide layer, which agrees to our previous statement that the oxide layer contains TiO_2 and Al_2O_3. Nb, Ta, and Cr are also seen in the oxide layer, indicating the compositional/phase complexity of the oxide layer. It is noted that the Al contents in the Al_2O_3 layer of $Al_{0.75}$ and $Al_{0.5}Zr_{0.01}$ are higher than that in $Al_{0.5}$, and $Al_{0.75}$ has relatively the best continuity of the Al_2O_3 layer, which is certainly beneficial for the oxidation resistance. However, a fully continuous and dense Al_2O_3 layer is not seen to form in any of these three RHEAs. In addition, cracks can be seen within the formed oxide layer in both $Al_{0.5}$ (Fig. 7(a)) and $Al_{0.75}$ (Fig. 7(i)), but not in $Al_{0.5}Zr_{0.01}$ (Fig. 7(q)). The cracking is generally due to the volumetric expansion mismatch among different formed oxides, and it seems that the Zr microalloying is effective in reducing the cracking trend in the $Al_{0.5}$ alloy, possibly because Zr microalloying helps either to reduce the volumetric expansion mismatch, or to enhance the bonding at interfaces among different oxides. The failure to form continuous and dense Al_2O_3 outermost layer together with the cracks formed among formed oxides are certainly deteriorating the oxidation resistance of these RHEAs, although the oxygen ingress below the oxide layer in all cases seems to be rather low even after 100 h of exposure (Fig. 7(h), (p) and (x)). The intermediate region is noticeably enriched in Ti and N, so it shall contain nitrides including

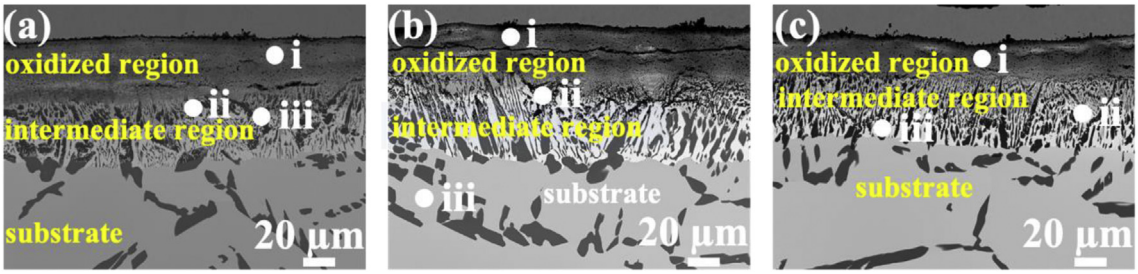

Fig. 6. Cross-sectional microstructures of (a) $Al_{0.5}$, (b) $Al_{0.75}$, and (c) $Al_{0.5}Zr_{0.01}$ specimens after 100 h of exposure at 1,100 °C.

Table 3
SEM–EDS analysis for the oxidized specimens after 100 h of exposure at 1,100 °C. The sampled locations are shown in Fig. 6(a), (b), and (c).

Composition	Element (at. %)							
Location	Al	Cr	Nb	Ta	Ti	N	O	Zr
$Al_{0.5}$								
i	34.75	0.04	0.26	0.43	10.2	4.6	49.72	–
ii	0.42	0.13	0.41	0.57	52.08	40.64	5.76	–
iii	12.61	3.03	14.54	15.1	12.23	16.61	25.88	–
$Al_{0.75}$								
i	27.81	0.21	4.16	0.31	7.04	–	60.47	–
ii	0.95	0.31	0.41	0.45	47.91	49.33	0.64	–
iii	16.5	8.21	14.33	14.86	39.78	–	6.33	–
$Al_{0.5}Zr_{0.01}$								
i	14.43	0.08	0.11	0.25	17.9	4.06	63.18	–
ii	14.33	3.66	15.91	14.59	23.03	23.43	4.96	0.09
iii	0.59	0.12	0.57	0.46	59.39	33.14	5.44	0.29

Ti_2N and TiN, as previously stated; elements Ti, Nb, Ta, Cr, and Al are also seen in this intermediate region, so it could also contain phases like Ti_2AlNb, alloyed with Ta and Cr [24]. Nitrides are also seen in the substrate, with blocky features. It is noted here that although nitrides are also seen to form in the substrate in $Al_{0.75}$ (Fig. 7(i)), the nitrogen content in the substrate of this alloy is significantly lower than that in the substrates of $Al_{0.5}$ and $Al_{0.5}Zr_{0.01}$, by comparing the N mapping in Fig. 7(g), (o), and (w).

To get a more accurate chemical distribution, EPMA elemental mapping was also made on two alloys with different Al contents: $Al_{0.5}$ (Fig. 8(a)–(h)) and $Al_{0.75}$ (Fig. 8(i)–(p)). Compared to the SEM–EDS elemental mapping results, the existence of multiple layers and the compositional complexity in the oxide layer is confirmed, so is the higher content of Al and the better continuity of the outer Al_2O_3 layer in $Al_{0.75}$ compared with those in $Al_{0.5}$. The much lower content of nitrogen in the substrate of $Al_{0.75}$ (Fig. 8(p)), compared with that in $Al_{0.5}$ (Fig. 8(h)), is also confirmed, thus further verifying that a higher Al content is effective in limiting the nitrogen ingress. Two new observations maybe added based on the EPMA element mapping results. First, nitrogen is also seen in the outer oxide layer, so chances are that nitrides could already form in the oxide layer, rather than only forming later in the intermediate region and the substrate below. Second, oxygen is still seen below the oxide layer in both $Al_{0.5}$ and $Al_{0.75}$, but its diffusion into the substrate stops at a short distance away from the oxide layer, and comparatively, it does so much quicker in $Al_{0.75}$ than in $Al_{0.5}$, lending further support to the positive role of a higher Al content in suppressing the oxygen ingress.

Adding additional evidence for the oxidation products, an EBSD phase map (Fig. 9(b)) was made on the cross-section (Fig. 9(a)) of the $Al_{0.75}$ alloy. It basically confirms the above-inferred information based on XRD, microstructural observation and compositional analysis in that Al_2O_3 forms the outer layer, but it is not the exclusively formed oxide layer at the surface because TiO_2 also forms there; TiO_2 constitutes the main oxide in the oxide layer, as although the $Al_{0.75}$ alloy contains lower Ti than that of $Al_{0.5}$, the amount of Ti in $Al_{0.75}$ is still high enough to form a thick TiO_2 layer, with TiO_2 being one of the most thermodynamically stable oxides (Fig. 9(c)); underneath the oxide layer, there is the intermediate region that contains Ti_2AlNb and the nitride TiN, interdiffused with the substrate bcc phase. Fig. 9(c) shows the standard Gibbs free energy of formation (per mole) for the thermodynamically stable oxides [35,38], that are related to the alloying elements in these RHEAs, together with that for TiN. After the initial oxidation to form TiO_2, with the prolonged exposure, further oxidation reactions take place with the remaining metal elements like Al and Nb forming subsequent oxide (Al_2O_3 and Nb_2O_5) and nitride (TiN).

4. Discussion

4.1. Internal oxidation and nitridation

The results obtained clearly indicate the positive effect of alloying Al and Zr on the oxidation resistance of the initial $Al_{0.5}$ alloy, with Al having the more significant effect. Nevertheless, all the three RHEAs experience internal oxidation at both 800 °C and 1,100 °C, indicating that the formed oxide scales are not sufficiently protective. There are possibly two main reasons for the insufficient oxidation resistance for these alloys, based on which further improvements can be made. First, these alloys contain a high concentration of reactive elements like Ti, Ta, and Nb, displaying significant oxygen solubility at elevated temperatures [39]. They would form oxides like TiO_2, Ta_2O_5, and Nb_2O_5, and therefore disallowing Al to form the exclusive Al_2O_3 scale, when the Al content has to be low to maintain the tensile ductility. The inability to form an exclusively protective oxide scale such as Al_2O_3, which is usually more effective against oxygen ingress than multilayered oxide scale such as mixed Al_2O_3 and TiO_2 [37], is fundamentally responsible for the insufficient oxidation resistance. Second, the formation of Nb_2O_5 and subsequently its reaction with TiO_2 to form $TiNb_2O_7$ leads to cracking (Fig. 7(a)), since Nb_2O_5 is one of the most expanding oxides that can promote crack formation at the interfaces between the different oxides or between the oxide layer and the intermediate region underneath [16,40,41], creating channels for rapid oxygen ingress. Nb_2O_5 goes through volume expansion on high-temperature exposure due to various polymorphic transformations (i.e. various monoclinic and orthorhombic Nb_2O_5 below 1,100 °C, and monoclinic Nb_2O_5 above 1,100 °C), and its formation is regarded as detrimental for the oxidation resistance [16]. Zr plays a positive role in relieving the cracking tendency, as seen in Fig. 7(q), whereas Al does not (Fig. 7(i)). On the other hand, Al has a positive role in enhancing the oxidation resistance of the $Al_{0.5}$ alloy. First and foremost, a higher Al content leads to the formation of a more continuous outer Al_2O_3 layer, which effectively inhibits the oxygen ingress (Table 3).

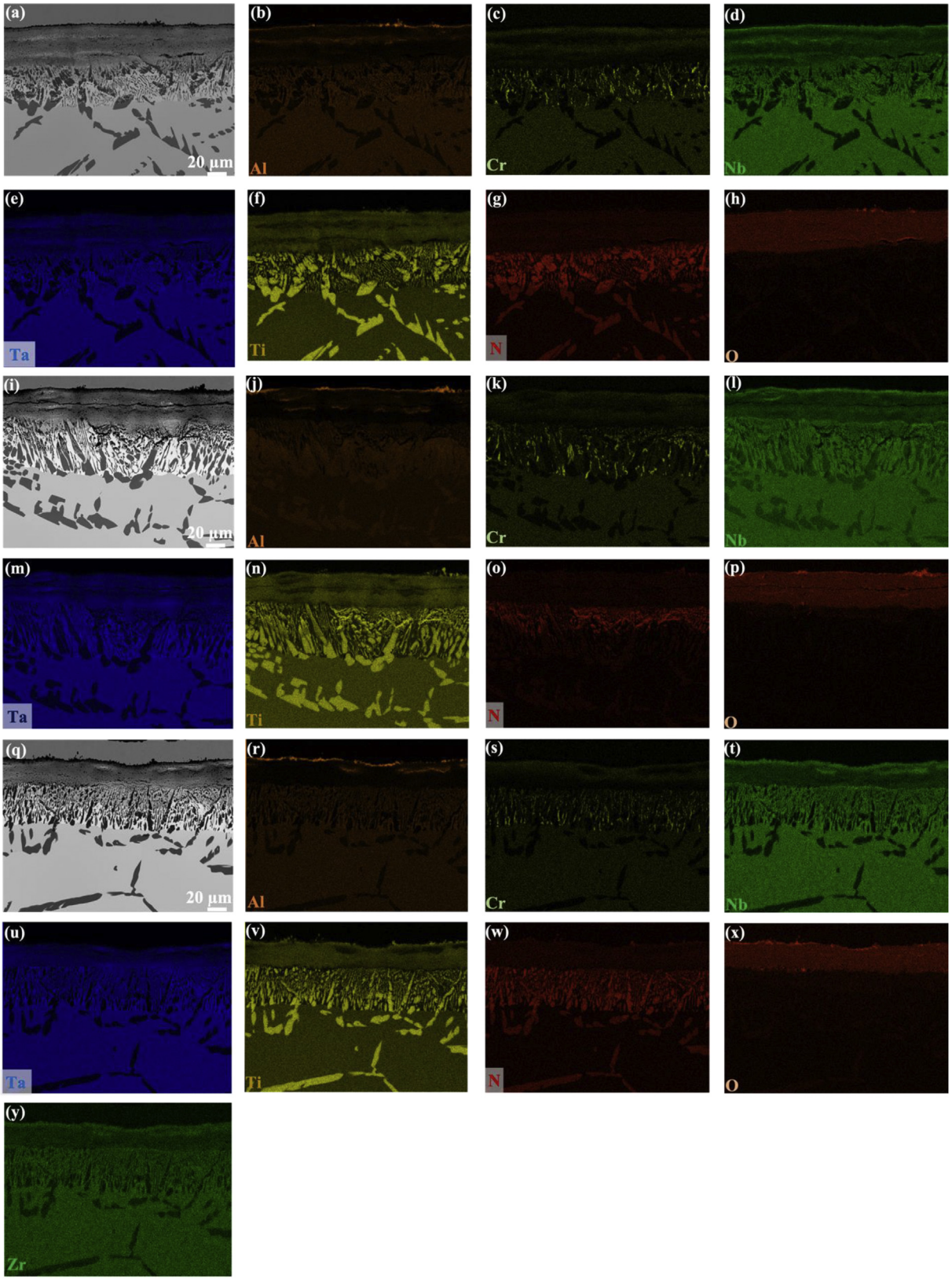

Fig. 7. Cross-sectional EDS elemental mapping of (b–h) $Al_{0.5}$, (j–p) $Al_{0.75}$, and (r–y) $Al_{0.5}Zr_{0.01}$ specimens after 100 h of exposure at 1,100 °C. The corresponding cross-sectional microstructures given in (a), (i), and (q) are the same as those shown in Fig. 6.

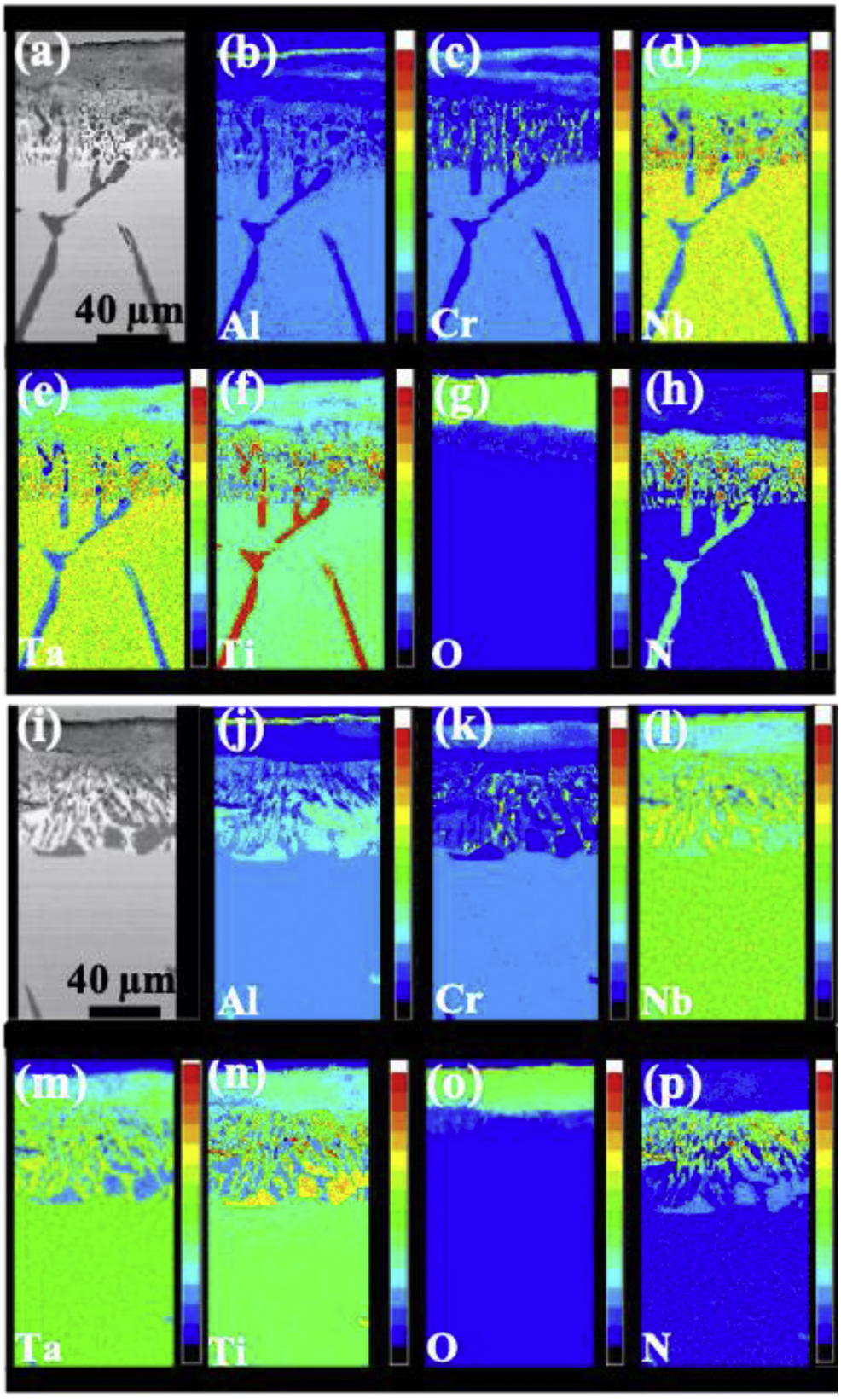

Fig. 8. Cross-sectional microstructures and EPMA elemental mapping of (a–h) $Al_{0.5}$ and (i–p) $Al_{0.75}$ specimens after 100 h of exposure at 1,100 °C.

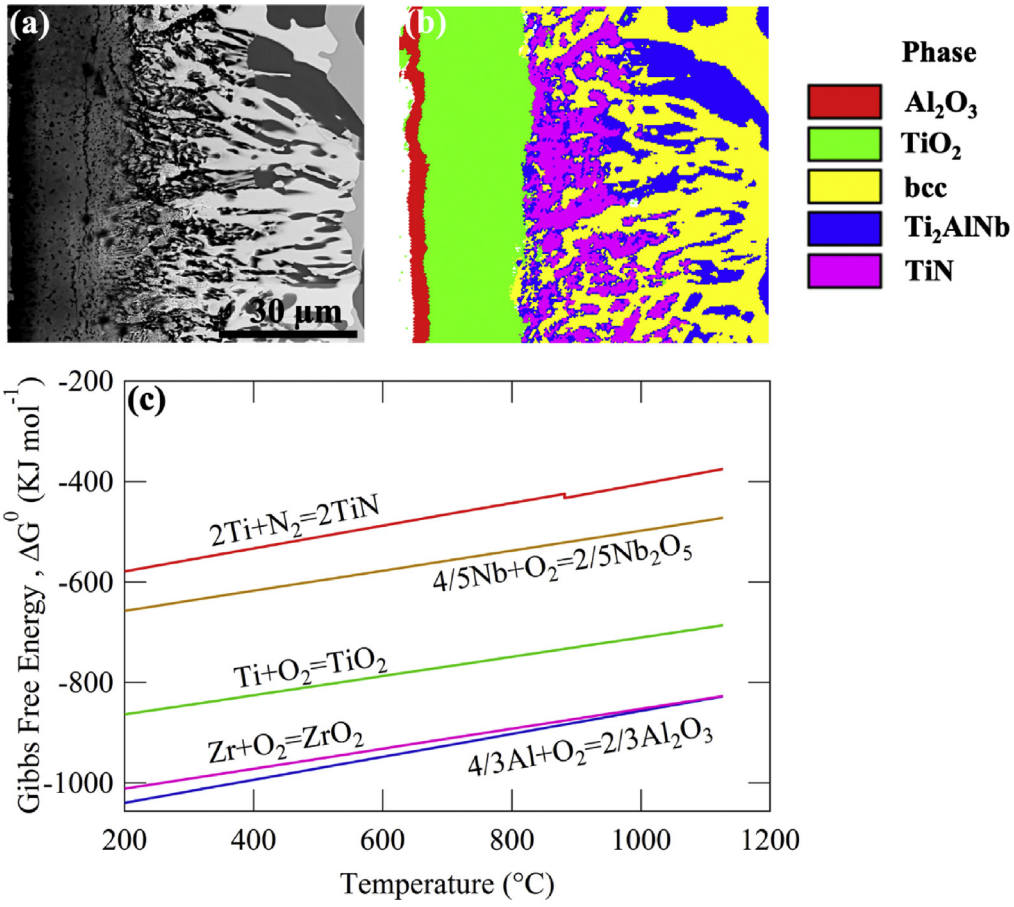

Fig. 9. (a) Cross-sectional microstructure and (b) corresponding EBSD phase map of $Al_{0.75}$ after 100 h of exposure at 1,100 °C, and (c) plot of standard Gibbs free energy of formation for relevant oxides and nitrides.

Second, as can be seen in Fig. 9(b), a higher Al content in $Al_{0.75}$ seems to suppress the formation of Nb_2O_5, which could otherwise cause the cracking issue and deteriorate the oxidation resistance.

As seen here in this work, nitridation is another concern for RHEAs in addition to oxidation, which has not been extensively studied when looking into the oxidation of RHEAs. Previously, nitrides that were seen in RHEAs mainly include TiN, AlN, Cr_2N, and Nb_2N. Using the NV1 alloy as an example [31], it forms nitrides TiN at both 1,000 °C and 1,100 °C, whereas AlN is formed at 1,100 °C, after 200 h of air exposure. These nitrides are formed because of the more rapid ingress of nitrogen than oxygen into the bulk of the material. It was also claimed that the preferential diffusion of nitrogen occurs via the Mo-rich region in this particular NV1 alloy, eventually promoting nitridation [31]. Another example is with AlCrNbMoTi, which at 1,000 °C is extremely prone to nitrogen ingress and forms three types of nitrides: TiN, Cr_2N, and Nb_2N, in addition to the very stable oxides, that is, Al_2O3 and TiO_2 [18]. Certainly, nitridation was also identified in other refractory elements containing materials, for example, in single-crystalline nickel-base Ni–Cr–Al–Ti superalloys, where the solubility and diffusion of nitrogen within Ni-base alloys increase with increasing Cr content, leading to the formation of TiN [42]. Therefore, in addition to oxidation, nitridation in RHEAs is an important subject for further studies. Encouragingly, Al seems to also play a positive role regarding the nitridation resistance, as the enhanced oxidation resistance because of a higher Al content in $Al_{0.75}$ simultaneously inhibits the nitrogen ingress, where only TiN is seen to form in the intermediate region (Fig. 9(b)) and no noticeable nitrides are seen to form in the substrate (Figs. 7 and 8).

4.2. Complex oxides

Recently, a complex oxide, $CrTaO_4$ [31,32], was proposed to act as a barrier for both inward diffusion of oxygen and outward diffusion of alloying elements in RHEAs. When comparing the oxidation resistance of the three RHEAs that are studied here with that of the other RHEAs at 1,100 °C, it was mentioned that the NV1 alloy shows much better performance and it was attributed to the formation of $CrTaO_4$ [31]. For the NV1 alloy, a weight gain of ~ 4.03 mg/cm^2 after 200 h of air exposure at 1,100 °C was reported, in contrast with a weight gain of 8.243 mg/cm^2 for $Al_{0.75}$ after 100 h of air exposure at the same temperature. The new type of protective oxide scale certainly looks promising. However, there exist also reports on the insufficient oxidation resistance of $CrTaO_4$, as is seen in AlCrMoNb [16], which was subject to oxidation at 1,000 °C. During initial oxidation, the formed oxide layer contains a mixture of Al_2O_3, Cr_2O_3, and $CrNbO_4$, but with prolonged exposure, porous and non-protective oxide scales are formed, resulting in complete material oxidation within 48 h. In another case of CrMoNbTaV, the complex oxides $CrNbO_4$ and $CrTaO_4$ completely vanished when the oxidation temperature was increased to 1,100 °C [43]. The seemingly conflicting results indicate that the effectiveness of complex oxides like $CrTaO_4$ is compositions dependent, which could be rationalized. It is well known that the oxidation resistance of alloys

is affected by the integrity of formed surface oxides when they are exposed to an oxidative atmosphere. Using thermally grown oxides, TGOs, as an example, the adhesive properties of TGOs can be determined by the CTE (coefficient of thermal expansion) mismatch between the surface oxide and substrate alloys, and the porosity in the TGOs might be altered by the water vapor pressure in the air. Therefore, further work is certainly requested to verify the suitable conditions where this type of complex oxide scale is effective in preventing RHEAs from oxygen (and nitrogen) ingress, over a wide temperature range and a long-term exposure. The point is that alloys forming such complex oxides can be used under circumstances where Al_2O_3 cannot be used as the protective oxide layer. Indeed, one type of complex oxide, $CoWO_4$, has been found effective as the protective oxide layer in the ferritic stainless steel interconnector parts [44,45]. The current work, nevertheless, indicates the possibility of protecting RHEAs from oxidation and nitridation, by forming the protective Al_2O_3 scale via the alloying route. Certainly, how to optimize the Al content to achieve a balance between tensile ductility and oxidation resistance, remains to be a great challenge for RHEAs. The dilemma of too little Al not leading to the formation of Al_2O_3 and too much Al causing embrittlement always exists, and therefore the alloy compositions need to be carefully adjusted to pinpoint the optimal Al content that can render the simultaneous achievement of tensile ductility (even a few percent could be acceptable) and oxidation resistance (ideally forming Al_2O_3).

5. Conclusions

The effect of alloying on the oxidation behavior of ductile RHEAs was studied, by comparing the oxidation resistance of a starting alloy, $Al_{0.5}Cr_{0.25}Nb_{0.5}Ta_{0.5}Ti_{1.5}$, with that of the two modified alloys, $Al_{0.75}Cr_{0.25}Nb_{0.5}Ta_{0.5}Ti_{1.5}$ and $Al_{0.5}Cr_{0.25}Nb_{0.5}Ta_{0.5}Ti_{1.5}Zr_{0.01}$, at 800 °C and 1,100 °C. Alloying of Al and Zr indeed enhances the oxidation resistance of $Al_{0.5}Cr_{0.25}Nb_{0.5}Ta_{0.5}Ti_{1.5}$, with Al having the more significant effect in inhibiting the oxygen ingress, whereas Zr plays a positive role in relieving the cracking trend in multilayered oxide scales. All the three RHEAs studied here show an excellent oxidation resistance at 800 °C compared with other RHEAs, although their performance at 1,100 °C awaits further improvements, mainly due to the failure to form protective oxide scales like an exclusive Al_2O_3 scale. Apart from oxidation, nitridation is found to be another concern for RHEAs and is closely related to oxidation. A higher Al content is beneficial to enhance both the oxidation and nitridation resistance.

Credit author statement

Saad Sheikh and Lu Gan: Experiments, Analysis, Discussion, Writing- original draft preparation; **Ayako Ikeda**: Analysis, Discussion, Writing- reviewing; **Hideyuki Murakami**: Supervision, Writing -reviewing; **Sheng Guo**: Supervision, Conceptualization, Analysis, Discussion, Writing-reviewing and editing.

Declaration of competing interest

The authors declare that they have no known competing financial interests or personal relationships that could have appeared to influence the work reported in this paper.

Acknowledgments

SS is grateful for the postdoc fellowship jointly supported by the Swedish Foundation for Strategic Research (SSF) and the Japanese Society for the Promotion of Science (JSPS). SG thanks the financial support from the ÅForsk Foundation (18-282).

References

[1] O.N. Senkov, G.B. Wilks, J.M. Scott, D.B. Miracle, Mechanical properties of $Nb_{25}Mo_{25}Ta_{25}W_{25}$ and $V_{20}Nb_{20}Mo_{20}Ta_{20}W_{20}$ refractory high entropy alloys, Intermetallics 19 (5) (2011) 698–706.
[2] O.N. Senkov, G.B. Wilks, D.B. Miracle, C.P. Chuang, P.K. Liaw, Refractory high-entropy alloys, Intermetallics 18 (9) (2010) 1758–1765.
[3] O.N. Senkov, D.B. Miracle, K.J. Chaput, J.-P. Couzinie, Development and exploration of refractory high entropy alloys-A review, J. Mater. Res. 33 (19) (2018) 3092–3128.
[4] J.W. Yeh, S.K. Chen, S.J. Lin, J.Y. Gan, T.S. Chin, T.T. Shun, C.H. Tsau, S.Y. Chang, Nanostructured high-entropy alloys with multiple principal elements: novel alloy design concepts and outcomes, Adv. Eng. Mater. 6 (5) (2004) 299–303.
[5] B. Cantor, I.T.H. Chang, P. Knight, A.J.B. Vincent, Microstructural development in equiatomic multicomponent alloys, Mater. Sci. Eng. A 375–377 (2004) 213–218.
[6] D. Miracle, O. Senkov, A critical review of high entropy alloys and related concepts, Acta Mater. 122 (2017) 448–511.
[7] J. Wadsworth, T.G. Nieh, J.J. Stephens, Recent advances in aerospace refractory metal alloys, Int. Mater. Rev. 33 (3) (1988) 131–150.
[8] D.M. Dimiduk, J.H. Perepezko, Mo-Si-B alloys: developing a revolutionary turbine-engine material, MRS Bull. 28 (9) (2003) 639–645.
[9] S. Sheikh, S. Shafeie, Q. Hu, J. Ahlstrom, C. Persson, J. Vesely, J. Zyka, U. Klement, S. Guo, Alloy design for intrinsically ductile refractory high-entropy alloys, J. Appl. Phys. 120 (2016) 164902.
[10] H. Huang, Y. Wu, J. He, H. Wang, X. Liu, K. An, W. Wu, Z. Lu, Phase-transformation ductilization of brittle high-entropy alloys via metastability engineering, Adv. Mater. 29 (30) (2017) 1701678.
[11] S. Sheikh, L. Gan, T.-K. Tsao, H. Murakami, S. Shafeie, S. Guo, Aluminizing for enhanced oxidation resistance of ductile refractory high-entropy alloys, Intermetallics 103 (2018) 40–51.
[12] S. Sheikh, M.K. Bijaksana, A. Motallebzadeh, S. Shafeie, A. Lozinko, L. Gan, T.-K. Tsao, U. Klement, D. Canadinc, H. Murakami, S. Guo, Accelerated oxidation in ductile refractory high-entropy alloys, Intermetallics 97 (2018) 58–66.
[13] O.N. Senkov, S.V. Senkova, D.M. Dimiduk, C. Woodward, D.B. Miracle, Oxidation behavior of a refractory $NbCrMo_{0.5}Ta_{0.5}TiZr$ alloy, J. Mater. Sci. 47 (18) (2012) 6522–6534.
[14] B. Gorr, M. Azim, H.J. Christ, T. Mueller, D. Schliephake, M. Heilmaier, Phase equilibria, microstructure, and high temperature oxidation resistance of novel refractory high-entropy alloys, J. Alloys Compd. 624 (2015) 270–278.
[15] D.J. Young, High Temperature Oxidation and Corrosion of Metals, Elsevier, Oxford, 2008.
[16] F. Mueller, B. Gorr, H.-J. Christ, J. Mueller, B. Butz, H. Chen, A. Kauffmann, M. Heilmaier, On the oxidation mechanism of refractory high entropy alloys, Corrosion Sci. 159 (2019) 108161.
[17] C.M. Liu, H.M. Wang, S.Q. Zhang, H.B. Tang, A.L. Zhang, Microstructure and oxidation behavior of new refractory high entropy alloys, J. Alloys Compd. 583 (2014) 162–169.
[18] B. Gorr, F. Mueller, H.J. Christ, T. Mueller, H. Chen, A. Kauffmann, M. Heilmaier, High temperature oxidation behavior of an equimolar refractory metal-based alloy 20Nb-20Mo-20Cr-20Ti-20Al with and without Si addition, J. Alloys Compd. 688 (2016) 468–477.
[19] B. Gorr, F. Mueller, M. Azim, H.-J. Christ, T. Mueller, H. Chen, A. Kauffmann, M. Heilmaier, High-temperature oxidation behavior of refractory high-entropy alloys: effect of alloy composition, Oxid. Metals 88 (3–4) (2017) 339–349.
[20] F. Mueller, B. Gorr, H.-J. Christ, H. Chen, A. Kauffmann, M. Heilmaier, Effect of microalloying with silicon on high temperature oxidation resistance of novel refractory high-entropy alloy Ta-Mo-Cr-Ti-Al, Mater. A. T. High. Temp. 35 (1–3) (2018) 168–176.
[21] Y.D. Wu, Y.H. Cai, T. Wang, J.J. Si, J. Zhu, Y.D. Wang, X.D. Hui, A refractory $Hf_{25}Nb_{25}Ti_{25}Zr_{25}$ high-entropy alloy with excellent structural stability and tensile properties, Mater. Lett. 130 (2014) 277–280.
[22] G. Dirras, L. Lilensten, P. Djemia, M. Laurent-Brocq, D. Tingaud, J.P. Couzinie, L. Perriere, T. Chauveau, I. Guillot, Elastic and plastic properties of as-cast equimolar TiHfZrTaNb high-entropy alloy, Mater. Sci. Eng. A 654 (2016) 30–38.
[23] O.N. Senkov, J.M. Scott, S.V. Senkova, D.B. Miracle, C.F. Woodward, Microstructure and room temperature properties of a high-entropy TaNbHfZrTi alloy, J. Alloys Compd. 509 (20) (2011) 6043–6048.
[24] S. Sheikh, L. Gan, X. Montero, H. Murakami, S. Guo, Forming protective alumina scale for ductile refractory high-entropy alloys via aluminizing, Intermetallics 123 (2020) 106838.
[25] O.N. Senkov, C. Woodward, D.B. Miracle, Microstructure and properties of aluminum-containing refractory high-entropy alloys, JOM 66 (10) (2014) 2030–2042.
[26] K. Zelenitsas, P. Tsakiropoulos, Study of the role of Al and Cr additions in the microstructure of Nb-Ti-Si in situ composites, Intermetallics 13 (10) (2005) 1079–1095.

[27] S. Matsunaga, A. Serizawa, Y. Yamabe-Mitarai, Effect of Zr on microstructure and oxidation behavior of alpha and alpha + alpha(2) Ti-Al-Nb alloys, Mater. Trans. 57 (11) (2016) 1902–1907.
[28] M. Yoshihara, Influence of Zr addition on oxidation behavior of TiAl-based alloys, Mater. Sci. Forum 696 (2011) 360–365.
[29] N. Birks, G.H. Meier, F.S. Pettit, Introduction to the High Temperature Oxidation of Metals, Cambridge University Press, Cambridge, 2006.
[30] R. Gawel, L. Rogal, K. Przybylski, Oxidation resistance of Ti-Al-Cr-Nb-based high-entropy alloys in air at 1073 K, J. Mater. Eng. Perform. 28 (7) (2019) 4163–4170.
[31] K.-C. Lo, Y.-J. Chang, H. Murakami, J.-W. Yeh, A.-C. Yeh, An oxidation resistant refractory high entropy alloy protected by $CrTaO_4$-based oxide, Sci. Rep. 9 (2019) 7266.
[32] B. Gorr, F. Müller, S. Schellert, H.-J. Christ, H. Chen, A. Kauffmann, M. Heilmaier, A new strategy to intrinsically protect refractory metal based alloys at ultra high temperatures, Corrosion Sci. (2020) 108475.
[33] J.M. Xiang, G.B. Mi, S.J. Qu, X. Huang, Z. Chen, A.H. Feng, J. Shen, D.L. Chen, Thermodynamic and microstructural study of Ti_2AlNb oxides at 800 ^{o}C, Sci. Rep. 8 (2018) 12761.
[34] J.R. DiStefano, B.A. Pint, J.H. DeVan, Oxidation of refractory metals in air and low pressure oxygen gas, Int. J. Refract. Metals Hard Mater. 18 (4) (2000) 237–243.
[35] T.M. Butler, K.J. Chaput, J.R. Dietrich, O.N. Senkov, High temperature oxidation behaviors of equimolar NbTiZrV and NbTiZrCr refractory complex concentrated alloys (RCCAs), J. Alloys Compd. 729 (2017) 1004–1019.
[36] J. Nowotny, Oxide Semiconductors for Solar Energy Conversion: Titanium Dioxide, CRC Press, Boca Raton, 2011.
[37] C. Leyens, M. Peters, Titanium and Titanium Alloys: Fundamentals and Applications, John Wiley & Sons, Weinheim, 2003.
[38] I. Barin, O. Knacke, O. Kubaschewski, Thermochemical Properties of Inorganic Substances: Supplement, Springer, Berlin, Heidelberg, 2013.
[39] E.M. Savitskii, G.S. Burkhanov, Physical Metallurgy of Refractory Metals and Alloys, Springer, Boston, MA, 1995.
[40] S.K. Varma, C. Parga, K. Amato, J. Hernandez, Microstructures and high temperature oxidation resistance of alloys from Nb-Cr-Si system, J. Mater. Sci. 45 (14) (2010) 3931–3937.
[41] J. Spyridel, P. Delavign, S. Amelinck, On superstructures of Ta_2O_5 and Nb_2O_5, Phys. Status Solidi 19 (2) (1967) 683. &.
[42] U. Krupp, H.J. Christ, Selective oxidation and internal nitridation during high-temperature exposure of single-crystalline nickel-base superalloys, Metall. Mater. Trans. A 31 (1) (2000) 47–56.
[43] Y.F. Xiao, W.H. Kuang, Y.F. Xu, L. Wu, W.J. Gong, J.W. Qian, Q.K. Zhang, Y.H. He, Microstructure and oxidation behavior of the CrMoNbTaV high-entropy alloy, J. Mater. Res. 34 (2) (2019) 301–308.
[44] L. Gan, H. Murakami, I. Saeki, High temperature oxidation of Co-W electroplated type 430 stainless steel for the interconnect of solid oxide fuel cells, Corrosion Sci. 134 (2018) 162–168.
[45] L. Gan, H. Murakami, T. Yamamoto, Microstructure and diffusion behavior in the multilayered oxides formed on a Co–W electroplated ferritic stainless steel followed by oxidation treatment, Acta Mater. 194 (2020) 295–304.